The Journal of Chemical Physics ARTICLE pubs.aip.org/aip/jcp

Using the Zeno line to assess and refine molecular models

Cite as: J. Chem. Phys. 160, 154503 (2024); doi: 10.1063/5.0192770
Submitted: 20 December 2023 • Accepted: 1 April 2024 •
Published Online: 16 April 2024

Thomas Paterson,[1,a)] Marcus N. Bannerman,[2] and Leo Lue[1]

AFFILIATIONS

[1] Department of Chemical and Process Engineering, University of Strathclyde, James Weir Building, 75 Montrose Street, Glasgow G1 1XJ, United Kingdom
[2] School of Engineering, University of Aberdeen, Aberdeen AB24 3UE, United Kingdom

[a)] **Author to whom correspondence should be addressed:** thomas.paterson@strath.ac.uk

ABSTRACT

The Zeno line is the locus of points on the temperature–density plane where the compressibility factor of the fluid is equal to one. It has been observed to be straight for a broad variety of real fluids, although the underlying reasons for this are still unclear. In this work, a detailed study of the Zeno line and its relation to the vapor–liquid coexistence curve is performed for two simple model pair-potential fluids: attractive square-well fluids with varying well-widths λ and Mie n-6 fluids with different repulsive exponents n. Interestingly, the Zeno lines of these fluids are curved, regardless of the value of λ or n. We find that for square-well fluids, $\lambda \approx 1.8$ presents a Zeno line, which is the most linear over the largest temperature range. For Mie n-6 fluids, we find that the straightest Zeno line occurs for n between 8 and 10. Additionally, the square-well and Mie fluids with the straightest Zeno line showed the closest quantitative agreement with the vapor–liquid coexistence curve for experimental fluids that follow the principle of corresponding states (e.g., argon, xenon, krypton, methane, nitrogen, and oxygen). These results suggest that the Zeno line can provide a useful additional feature, in complement to other properties, such as the phase envelope, to evaluate molecular models.

I. INTRODUCTION

The forces that act between molecules of real fluids are exceptionally complex multi-body interactions, and yet the thermodynamic properties of pure fluids exhibit many interesting "simple" regularities, such as the law of rectilinear diameter[1,2] and the law of corresponding states introduced initially by van der Waals and later extended by Pitzer and co-workers.[3,4] This work considers another regularity known as the Zeno line, which is the locus of thermodynamic states with a unit compressibility factor, Z, in the temperature–density plane. In general, the Zeno line need not be straight; however, experimentally, it has been observed to be very nearly straight for a large number of fluids.[5,6] To illustrate this, the Zeno line for argon, xenon, krypton, methane, nitrogen, and oxygen (the so-called corresponding-state fluids) is represented in Fig. 1 as gray dashed lines in the reduced absolute temperature T and number density $\rho = N/V$ plane. For typical systems, the Zeno line extends from the Boyle temperature T_B at zero density and terminates just above the triple point where it intersects the liquid–solid freezing curve. If the Zeno line were perfectly straight, then its extrapolation to zero temperature appears to be at a density ρ_B. The value of ρ_B for Mie and square-well fluids is determined here from the temperature dependence of the second and third virial coefficients of the system (see Sec. II); however, it is often determined empirically in experimental or numerical work. These real fluids obey the principle of corresponding states, meaning that their thermodynamic properties are found to be remarkably similar when scaled by their critical values.[7] The classic scaling by the critical temperature and density highlights the similarity of the phase envelope of these real fluids [see Fig. 1(a)], while the scaling by the Boyle temperature and density in Fig. 1(b) highlights the similarity of the Zeno lines and yields a 45° Zeno line. Both plots allow for an easy comparison of the agreement of a molecular model against these two features of real fluids.

The underlying physical reason for the linearity of the Zeno line is not fully understood; however, there has been some geometrical analyses on the relationship between the Zeno line and the line of rectilinear diameter,[14,15] as well as investigations into

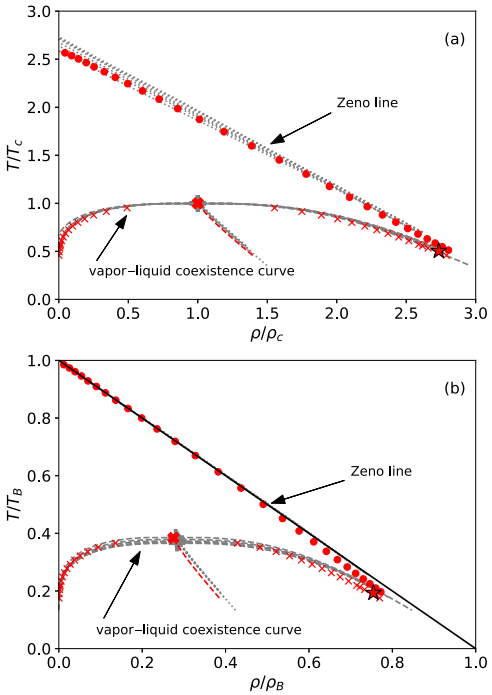

FIG. 1. The Zeno line and vapor–liquid coexistence curve for the corresponding state fluids (gray dashed lines) and the Lennard-Jones 12-6 potential (red symbols) scaled by the critical properties (a) and scaled by the Zeno line properties (b). Due to the large degree of overlap between different fluids, the dashed lines appear to be solid. The data for the corresponding states fluids were taken from the NIST Chemistry WebBook.[8] The phase equilibrium data for the Lennard-Jones fluid are taken from the NIST Standard Reference Simulation Website[9] for the 5σ truncation, and the Zeno line data are taken from the work of Urschel and Stephan.[10] For the corresponding state fluids, the ratio of critical temperature to the Boyle temperature was found to range from $T_c/T_B \approx 0.37$–0.38, and the ratio of the critical density is $\rho_c/\rho_B \approx 0.28$–$0.29$; thus, the large gray pluses denote the critical points of these fluids. For the LJ fluid, the critical point is located at[11] $k_B T_c/\varepsilon = 1.3120(7)$ and $\rho_c\sigma^3 = 0.316(1)$. This gives a value of $T_c/T_B \approx 0.384$ and $\rho_c/\rho_B \approx 0.275$. The red star denotes the triple point for the LJ system, which is located at[12,13] $k_B T_t/\varepsilon = 0.661$ and $\rho\sigma^3 = 0.864$.

other Zeno-like lines throughout the T–ρ plane.[16–18] The van der Waals equation of state (EOS) predicts a perfectly straight Zeno line.[19] Commonly used EOSs that are derived from it, such as the Redlich–Kwong–Soave and Peng–Robinson equations of state, are able to approximately predict the Zeno line of real fluids with reasonable accuracy,[20] implying that they sufficiently capture some intrinsic behavior of the real fluid. Furthermore, the Zeno line has been used to improve semi-empirical equations of state,[20–22] suggesting that the Zeno line may also be a necessary feature of any model molecular fluid. In this way, a straight Zeno line provides an interesting additional basis on which such models may be evaluated, beyond the examination of the phase envelope, which of course must also remain well captured.

While many real fluids exhibit straight Zeno lines, the same is not true for model molecular fluids. Recently, there has been renewed interest in the Zeno line for fluids modeled with pair-potentials using molecular simulation.[16,23–27] Perhaps the most widely used model is the Mie potential where the interparticle energy, $u(r)$, as a function of interparticle distance r is given by the following expression:

$$u(r) = \frac{n\,\varepsilon}{n-m}\left(\frac{n}{m}\right)^{m/(n-m)}\left[\left(\frac{\sigma}{r}\right)^{n} - \left(\frac{\sigma}{r}\right)^{m}\right], \tag{1}$$

where σ is the particle diameter and ε is the interaction energy. The use of this potential is widespread, particularly where the free parameters are set to $n = 12$ and $m = 6$, which is also known as the Lennard-Jones (LJ) 12-6 fluid. Deiters and his coworkers[10,28,29] have performed an exhaustive study of the characteristic curves of the Lennard-Jones 12-6 fluid. The Zeno line for the LJ 12-6 fluid (also presented in Fig. 1) is relatively straight at high-temperatures/low-densities, but the deviation at low-temperatures/high-densities is significant when compared to the Zeno line of real fluids. Similarly, the vapor–liquid coexistence curve for the LJ 12-6 fluid (the red crosses in Fig. 1) is also similar to that of the corresponding-states; however, the deviation at low and high temperatures is also easily discernible. As mentioned, many real fluids exhibit a straight Zeno line; therefore, it is not unreasonable to desire that the foundational molecular models used to construct more "realistic" potentials or theoretical descriptions should be able to reproduce this behavior. They must do this and more if they are to agree with the behavior of real fluids over the entire range of temperature and density/pressure.

In addition to the Mie potential, the particularly simple square-well fluid has been shown to present a *curved* Zeno line for a particular set of model parameters,[24] but a full exploration has not taken place. In square-well systems, the particles interact with each other through a potential of the following form:

$$u(r) = \begin{cases} +\infty & \text{for } 0 < r < \sigma, \\ -\varepsilon & \text{for } \sigma < r < \lambda\sigma, \\ 0 & \text{for } \lambda\sigma < r. \end{cases} \tag{2}$$

The particles are hard spheres with diameter σ that interact with each other through an attractive square-well of depth ε and width $\lambda\sigma$. This potential, while simple, possesses the key elements of excluded volume and an attractive interaction at intermediate distances. The square-well model is fundamentally interesting as it is at the heart of several thermodynamic perturbation theories. In addition, there exists an exact virial expansion up to the third coefficient[30] with an empirical expression for the fourth,[31] and no truncation of the potential profile is required for simulation, unlike the Mie fluids. This also facilitates a theoretical examination of the Zeno line as a basis of comparison against simulation results. Here, an in-depth examination of the Zeno line for the square-well fluids is carried out. The first objective is to discern whether the curved Zeno line is the general case for this model. Once this is established, it is observed whether the curvature of Zeno line has implications for other properties of the fluid. In general, by observing the set of conditions for which the Zeno line is not straight, it may be possible to offer some insights into why, for so many real fluids, it is.

The remainder of this paper is organized as follows. In Sec. II, the behavior of the Zeno line in the low density limit is examined based on the virial expansion. In Sec. III, the details of the molecular simulation methods used in this work are described. In particular,

the event molecular dynamics simulations and the methods used to locate the Zeno line are described, along with the multicanonical Monte Carlo simulations used to determine vapor–liquid phase coexistence. The Zeno lines for square-well fluids of different well-widths and Mie fluids of repulsive exponents are then examined and discussed. In Sec. V, the vapor–liquid coexistence curves of square-well and Mie fluids are analyzed. Finally, the main findings of this work are summarized in Sec. VI, along with directions for future research.

II. VIRIAL EXPANSION FOR THE ZENO LINE

In this section, theoretical estimates for the properties of the Zeno line are determined. At very low densities, the thermodynamic properties of a fluid are well approximated by the virial expansion,[24,32,33] where the deviation of the equation of state from that of the ideal gas can be expanded in a Taylor series in density around zero density as follows:

$$\frac{\beta p}{\rho} = 1 + B_2(T)\rho + B_3(T)\rho^2 + B_4(T)\rho^3 + \cdots, \tag{3}$$

where p is the pressure, $\beta = (k_B T)^{-1}$ is the inverse temperature, $B_2(T)$ is the second virial coefficient, $B_3(T)$ is the third virial coefficient, and so on. The virial coefficients are independent of density, but, in general, they will depend on the absolute system temperature, $k_B T$.

At very low densities, the dependence of the temperature of the Zeno line on the density can be expanded in a power series as follows:

$$\frac{T(\rho)}{T_B} \approx 1 - \frac{\rho}{\rho_B} + K\left(\frac{\rho}{\rho_B}\right)^2 + \cdots, \tag{4}$$

where ρ_B and K are considered to be parameters to be determined. The parameter ρ_B relates to the slope of the tangent of the Zeno line at the Boyle temperature, while the parameter K is related to the curvature of the Zeno line at the Boyle temperature. If the above expansion for $T(\rho)$ is inserted into Eq. (3), set $\beta p/\rho = 1$, and all terms are expanded and collected into a power series in ρ; the following series is found:

$$\begin{aligned} 0 &\approx B_2(T)\rho + B_3(T)\rho^2 + B_4(T)\rho^3 + \cdots \\ &\approx \left[B_2(T_B) + B_2'(T_B)T_B\left(-\frac{\rho}{\rho_B} + K\left(\frac{\rho}{\rho_B}\right)^2 + \cdots\right)\right. \\ &\quad \left. + \frac{1}{2}B_2''(T_B)T_B^2\left(-\frac{\rho}{\rho_B} + \cdots\right)^2 + \cdots\right]\rho \\ &\quad + \left[B_3(T_B) + B_3'(T_B)T_B\left(-\frac{\rho}{\rho_B} + \cdots\right) + \cdots\right]\rho^2 \\ &\quad + B_4(T_B)\rho^3 + \cdots. \end{aligned} \tag{5}$$

Collecting terms of the same order in ρ,

$$\begin{aligned} 0 \approx\ & B_2(T_B)\rho + \left[B_3(T_B)\rho_B - B_2'(T_B)T_B\right]\frac{\rho}{\rho_B}\rho \\ &+ \left[B_2'(T_B)T_B K + \frac{1}{2}B_2''(T_B)T_B^2 - B_3'(T_B)T_B\rho_B^2\right. \\ &\left. + B_4(T_B)\rho_B^2\right]\left(\frac{\rho}{\rho_B}\right)^2\rho + \cdots. \end{aligned} \tag{6}$$

The coefficients of each power of the density should be zero along the Zeno line. Zeroing the first term leads to the definition of the Boyle temperature, T_B, which is the temperature at which the leading/second virial coefficient vanishes [i.e., $B_2(T_B) = 0$]. This is not particularly interesting as it can also be determined directly from the virial expansion of Eq. (3). Continuing, the second order term leads to an analytical expression for the density ρ_B,

$$\rho_B = \frac{B_2'(T_B)}{B_3(T_B)}T_B, \tag{7}$$

where the prime denotes a derivative in temperature. This expression for ρ_B was first derived by Holleran[33] and explicitly given for the square-well potential by Apfelbaum and Vorob'ev.[24] While the square-well fluid is explored in a moment, Eq. (7) does allow for the calculation of the Zeno density for the LJ 12-6 fluid, giving the result $\rho_B\sigma^3 = 1.147$.

Finally, zeroing the third order term in Eq. (6) leads to an expression for the curvature K of the Zeno line at the Boyle temperature/zero-density,

$$K = \frac{1}{B_2'(T_B)T_B}\left[-\frac{1}{2}B_2''(T_B)T_B^2 + B_3'(T_B)T_B\rho_B - B_4(T_B)\rho_B^2\right]. \tag{8}$$

We believe this to be a new result, which allows the curvature of the Zeno line at zero density to be estimated within the precision of the virial terms. If the Zeno line is completely straight, it must also begin as a straight line; thus, this expression can be used to search for more "realistic" potentials and their parameters. When Eq. (8) is applied to the LJ 12-6 system, it yields a curvature value of $K = -0.009\,975$. This highlights that the LJ 12-6 system does not exhibit an exactly straight Zeno line, even for low densities. This contradicts earlier reports based on simulation exploration,[16] although it must be said the virial approach here allows for greater precision in determining this initial curvature.

The Zeno line properties at the Boyle temperature for attractive square-well fluids of different well widths and Mie n-6 fluids with varying n are plotted in Fig. 2 to explore the effect of their parameters on these properties. To calculate these parameters for the square-well interaction potential, exact expressions for the second and third virial coefficients[34–36] are used. There are no exact analytic expressions for higher order virial coefficients, but accurate empirical approximations have been developed by fitting numerical calculations and are available for the fourth- to ninth-order virial coefficients[31,37–40] for well-widths in the range $1.2 \le \lambda \le 2$. The empirical expression for the fourth virial coefficient used here is taken from Ref. 31, and it is repeated in the Appendix for completeness. The exact expression for the Boyle temperature for square-wells can be determined from the second virial to be as follows:

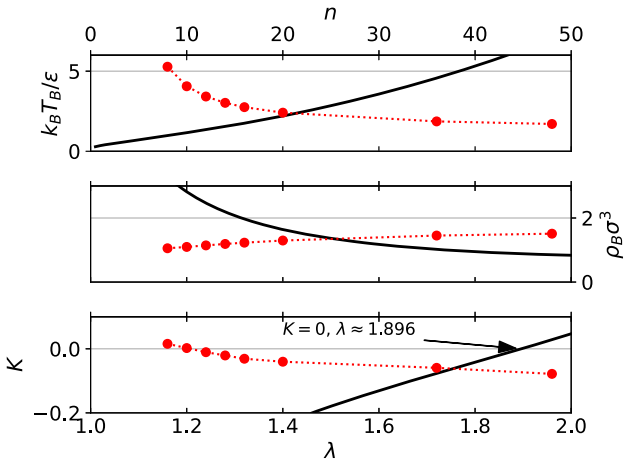

FIG. 2. Properties of the Zeno line near the Boyle temperature and zero density for square-well (black solid lines) and Mie n-6 (red filled circles) systems. (Top) Boyle temperature T_B, (middle) Zeno density ρ_B, and (bottom) curvature of the Zeno line K.

$$\frac{k_BT_B}{\varepsilon} = \left[\ln\frac{\lambda^3}{\lambda^3-1}\right]^{-1}. \tag{9}$$

As can be seen, the Boyle temperature monotonically increases with the decreasing well-width for the square-well fluid. As λ increases, the square-well Boyle temperature, scaled by ε/k_B, also increases; this reflects the greater interaction "volume" for particles with a larger well width, which leads to more attractive interactions that require a higher temperature to overcome.

The Zeno line density, ρ_B, for square wells can also be determined exactly and is plotted in Fig. 2. It decreases with the increasing well width, becoming fairly level at high values of λ and diverging as $\lambda \to 1$. Finally, the curvature at zero density of the Zeno line K for square wells is determined using approximate expressions for the fourth virial in Fig. 2. If $K < 0$ (i.e., $\lambda < 1.896$), the Zeno line initially curves downward from the Boyle temperature at zero density, while if $K > 0$ ($\lambda > 1.896$), it initially curves upward. The case $K = 0$ corresponds to an initially straight Zeno line ($\lambda \approx 1.896$). This analysis is in agreement with that of Apfelbaum and Vorob'ev[24] in that the Zeno line for the square well fluid is not straight in the low density region for a general value of λ; however, the best candidate well-width of $\lambda \approx 1.896$ for a straight Zeno line has been identified.

The same analysis for the Zeno line parameters for various Mie n-6 fluids is carried out and summarized in Table I. They are also displayed as the red filled circles in Fig. 2 for comparison against the square well system. In this work, the analysis is limited to Mie fluids with $m = 6$, as this has some physical basis in long-range decay of the attractive dispersion interaction between atoms.

The author of Ref. 41 provided an exact expression for the second virial coefficient for the LJ 12-6 potential and approximate expressions for the values of the third and fourth virial coefficients. In addition, tables for the values of the second and third virial coefficients as a function of temperature are provided in the supplementary material of Ref. 29. For the general Mie n-6 potential, the second virial coefficient and its first and second derivatives

TABLE I. Zeno line parameters for fluids interacting with the Mie n-6 potential.

n	k_BT_B/ε	$\rho_B\sigma^3$	K
8	5.278	1.0553 ± 0.0002	0.015 67 ± 0.000 56
10	4.058	1.0970 ± 0.0002	0.002 36 ± 0.000 33
11	3.695	1.1208 ± 0.0001	−0.004 50 ± 0.001 26
12	3.418	1.1446 ± 0.0006	−0.010 51 ± 0.001 47
14	3.023	1.1890 ± 0.0003	−0.019 58 ± 0.001 41
16	2.754	1.2301 ± 0.0003	−0.031 82 ± 0.001 70
20	2.409	1.2968 ± 0.0003	−0.040 36 ± 0.001 16
36	1.864	1.4518 ± 0.0001	−0.059 40 ± 0.002 38
48	1.704	1.5102 ± 0.0003	−0.078 22 ± 0.002 57

were determined via quadrature and series expansion.[42] The third and fourth virial coefficients were computed using Mayer-sampling Monte Carlo.[43] The Boyle temperatures for the Mie fluids were taken from Ref. 44.

For the LJ 12-6 potential, the Boyle temperature is calculated to be $k_BT_B/\varepsilon \approx 3.4179$. The Boyle temperature decreases with increasing n, which corresponds to increasing the stiffness of the repulsive core of the interaction potential, while the Zeno density ρ_B increases. The curvature K of the Zeno line at zero density decreases with increasing n. For $n = 8$, the curvature is positive, while for $n > 11$, the curvature is negative. The curvature will be zero somewhere between $n = 10$ and 11. With the exception of this particular value of n, none of the Mie n-6 fluids is expected to have a Zeno line that is perfectly straight.

Other properties along the Zeno line can be explored, such as the configurational energy and heat capacity. Within the virial expansion, the configurational energy is given by the following expression:

$$U^{\rm res} \approx -k_BT^2\left[B_2'(T)\rho + \frac{1}{2}B_3'(T)\rho^2\frac{1}{3}B_4'(T)\rho^3 + \cdots\right]. \tag{10}$$

To first order in the density, the configurational energy along the Zeno line should therefore vary as follows:

$$\begin{aligned} U^{\rm res} &\approx -\varepsilon\lambda^3 B_2^{\rm HS}\rho + \cdots \\ &\approx -\varepsilon\frac{2\pi\lambda^3}{3}\rho\sigma^3 + \cdots. \end{aligned} \tag{11}$$

The residual heat capacity, which is the derivative of the interaction energy with temperature, is given by the following expression:

$$\begin{aligned} C_V^{\rm res} \approx -k_BT\Big[&[2B_2'(T) + TB_2''(T)]\rho + \frac{1}{2}[2B_3'(T) + TB_3''(T)]\rho^2 \\ &+ \frac{1}{3}[2B_4'(T) + TB_4''(T)]\rho^3 + \cdots\Big]. \end{aligned} \tag{12}$$

To first order in density, the variation of the heat capacity along the Zeno line is as follows:

$$\begin{aligned} C_V^{\rm res} &\approx -k_BT_B[2B_2'(T_B) + T_BB_2''(TB)]\rho + \cdots, \\ \frac{C_V^{\rm res}}{k_B} &\approx \left(\frac{\varepsilon}{k_BT_B}\right)^2\lambda^3 B_2^{\rm HS}\rho + \cdots. \end{aligned} \tag{13}$$

Note that as the expressions given in Eqs. (11) and (13) are truncated to first order in density, they are linear; the neglected higher order terms will lead to the curvature of these properties with density.

These expressions are used later to provide a basis of comparison when exploring the simulation results. In Sec. III, details of the simulations used to locate the Zeno line and vapor–liquid coexistence curves for square-well fluids are given. The simulation results can be used to verify these results, confirm if the square-well has a straight Zeno line, and to explore its other properties.

III. SIMULATION DETAILS

To determine the Zeno line's location for all densities/temperatures, event driven molecular dynamics (EDMD) simulations in the NVT ensemble for systems of attractive square-well particles are carried out using the DynamO[45] software. For the square-well system, the pressure can be calculated directly from the core and bounce event rates, $\dot{\mathcal{N}}_{\text{core}}$ and $\dot{\mathcal{N}}_{\text{bounce}}$, respectively, using the following relation:[46]

$$Z = 1 + \frac{(\pi\beta m\sigma^2)^{1/2}}{3N}(\dot{\mathcal{N}}_{\text{core}} - \lambda\dot{\mathcal{N}}_{\text{bounce}}). \tag{14}$$

This expression implies that along the locus of points where $Z = 1$ (i.e., the Zeno line), the two event rates cancel; thus, $\dot{\mathcal{N}}_{\text{core}} = \lambda\,\dot{\mathcal{N}}_{\text{bounce}}$. A total of $N = 864$ particles were used for each simulation, initially arranged in an FCC lattice with random initial velocities and equilibrated for 10^2N events. Each simulation was then permitted to run for further 10^2N production events, and this was repeated three times to collect statistics, and the reported results were averaged over these three runs. Simulations were used to bracket the Zeno line density to within $\pm 0.02\rho_B$ around $Z = 1$ for each well width. Estimates for the Zeno state-points were made in intervals between $0.8T/T_B$ and $0.15T/T_B$. These simulations performed were then used to determine isotherms around the density at which $Z = 1$. For each isotherm, this procedure gives precise data for Z across a narrow range of densities, which brackets the density where $Z = 1$. This dataset for Z as a function of ρ was then fit to a quadratic polynomial using the UltraNest Bayesian inference package.[47–49] Based on this fit, the density at which $Z = 1$ is estimated, and the uncertainty of this estimate is also determined by propagating the posterior estimates at the fitted Zeno density. Other properties, such as the configurational internal energy and heat capacity, are calculated in a similar manner using the posterior distribution of each respective property fitted to density at isothermal state-points bracketing the Zeno density. This distribution is then evaluated at the Zeno density to give the property along the Zeno line.

In order to determine the vapor–liquid coexistence curves for square-well fluids of different well widths, multicanonical simulations[50–52] are performed with cubic simulation boxes of side lengths $L = 7\sigma$, 10σ, 12σ, and 15σ with periodic boundary conditions. For each system size at each temperature, the simulations are begun with an empty box and a flat multicanonical weight. Each individual simulation run consists of 10^7 attempted insertion/deletion moves and 10^7 attempted displacement moves. Based on the results of the simulation, the multicanonical weights are updated after each run to allow for uniform sampling of the number of particles in the system. The initial runs gradually increase the maximum number of particles allowed in the system; this facilitates the determination of the multicanonical weights. Once the freezing density is reached, simulation runs are repeated in batches of ten until the frequency of observed particle numbers in the system is uniform to an acceptable level. From the multicanonical weights, the density histograms can be determined for any chemical potential. The vapor–liquid coexistence point is determined by searching for the chemical potential where the density histogram has two peaks (one corresponding to the vapor phase and the other to the liquid phase) with an equal area.

IV. SIMULATION RESULTS FOR THE ZENO LINE

A. Square-well fluids

The simulation results for the Zeno lines of square-well fluids of differing well-widths are shown in Fig. 3. The temperature is scaled by the Boyle temperature T_B, and the density is scaled by ρ_B, as determined from the virial expansion results in Eq. (7). The primary observation is that none of the square-well Zeno lines are straight. Even the initially straight line of $\lambda = 1.896$ identified using the virial approach begins to curve at higher densities. From the previous analysis of the viral expansion in Sec. II, all the Zeno lines for square-well fluids with $\lambda > 1.896$ will initially curve upwards from the Boyle temperature at low densities. Indeed, this is observed in Fig. 3, and these well-widths remain above the 45° line. For square-well fluids with $\lambda < 1.896$, the Zeno lines are expected to initially curve downwards from the Boyle temperature at low densities, and this is observed from the simulation data; however, all the Zeno lines begin to curve upwards at higher densities (lower temperatures).

Although not straight, one well-width which approximately follows the linear Zeno line for largest range of temperatures is $\lambda \approx 1.8$, as demonstrated in Fig. 3. It is shown later that this well-width also approximates the critical properties and phase envelope reasonably well. The Zeno lines of the square-well fluids that are closest to the

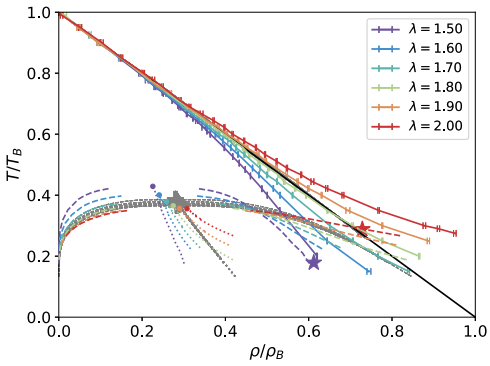

FIG. 3. The Zeno line (i.e., locus of points with $Z = 1$) for attractive square-well fluids of varying well width λ (colored solid lines) and real/corresponding-states fluids (gray solid lines). T_B is the Boyle temperature [see Eq. (9)], and ρ_B is the Zeno density [see Eq. (7)]. The dashed lines denote the boundaries of the vapor–liquid coexistence regions, and the dotted lines are the rectilinear diameters. The filled circles are the critical points for the square-well fluids, while the gray plus is the critical point for the corresponding states fluids. The red star denotes the triple point[53] for the square-well system with $\lambda = 2$, and the purple star denotes the triple point[54] for $\lambda = 1.5$.

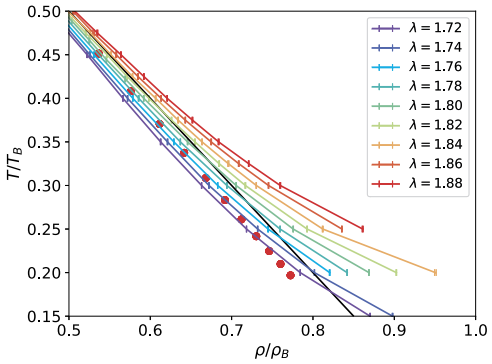

FIG. 4. The Zeno line for attractive square well fluids as in Fig. 3 for a narrower range of well-width $\lambda = 1.72$ to $\lambda = 1.88$ and smaller range to highlight the deviation of the LJ 12-6 and square-well fluids. The red circles denote the points on the Zeno line for the Lennard-Jones 12-6 potential. The black line is the ideal Zeno line. The gray solid lines are the Zeno lines for the corresponding states fluids.

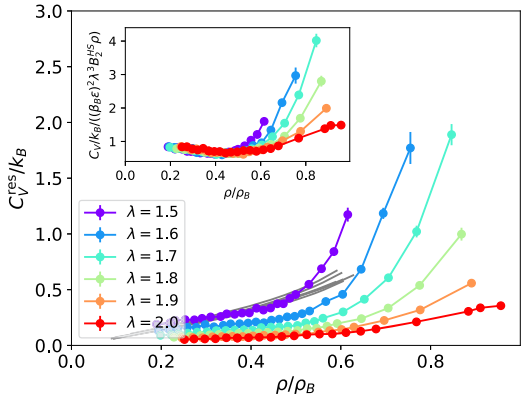

FIG. 6. Variation of the residual isochoric heat capacity along the locus of points with $Z = 1$ for attractive square-well fluids of varying well width λ (filled circles) and the corresponding states fluids (gray lines). ρ_B is the Zeno density [see Eq. (7)]. Inset: Reduced heat capacity [see Eq. (13)] along the Zeno line.

straight 45° line are shown in more detail at the lower temperatures in Fig. 4. As a comparison, the Zeno lines for the LJ 12-6 fluids are shown as the red filled circles. While a reasonable approximation of the real-fluid Zeno line is possible, neither the LJ 12-6 nor any variant of the square-well fluid avoids significant curvature at high-densities/low-temperatures; thus, some other key feature than attraction distance must be explored and adjusted to improve the agreement.

At very low densities, the systems closely resemble that of the ideal gas, which has $Z = 1$. This implies that only the locus of points with $Z = 1$ (i.e., the Zeno line) will intersect the Boyle temperature at $\rho = 0$. Although ideal gases have $Z = 1$, not all gases with Z of unity are necessarily ideal. Other properties, such as internal energy or entropy, can vary, making the fluid non-ideal. In Fig. 5, the variation of the configurational energy, scaled by the Boyle temperature, of square-well fluids with different values of λ along the Zeno line is plotted. These curves appear to be fairly straight, more so than the

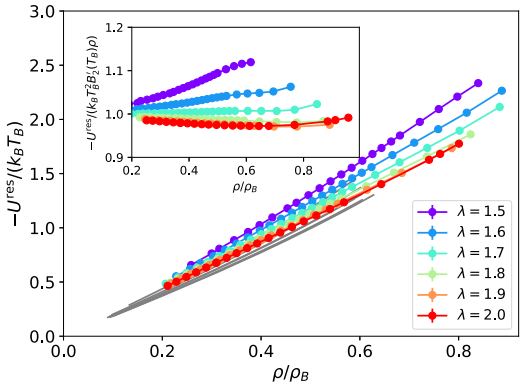

FIG. 5. Variation of the configurational energy along the locus of points with $Z = 1$ for attractive square-well fluids of varying well width λ (filled circles) and the corresponding states fluids (gray lines). Inset: Same plot with reduced configurational energy according to Eq. (11) to highlight the differences in curvature in the main plot.

corresponding Zeno lines in Fig. 3. The slope of these lines gradually decreases as λ increases, with the curves of the larger values of λ nearly overlapping. There is, however, a slight positive curvature in the data, with smaller values of λ curving upwards and the larger values of λ curving downwards. This is made more apparent by scaling the configurational energy by the factor $\lambda^2 B_2^{HS}\rho$, as suggested by Eq. (11) and shown in the inset in Fig. 5. The gray lines in Fig. 5 are the configurational energies for the various corresponding states fluids along the Zeno line. These lines are fairly straight and are all close to each other. They have a lower slope than all the square well systems and are closest to the $\lambda = 2$ system. This is another interesting feature that the square-well fluid fails to reproduce regardless of well-width.

The variation of the residual isochoric heat capacity of square well fluids along the Zeno line is shown in Fig. 6. The residual heat capacities are not linear, but they do seem to begin with a fairly straight region at low densities that abruptly curve upwards at a particular density. These curves shift to lower values and become more straight as the well-width λ increases. In the inset, the heat capacity is plotted in a manner suggested by Eq. (13). The gray lines in Fig. 6 are the residual isochoric heat capacities for the various corresponding states fluids. These lines are relatively straight and are grouped fairly close together, but they are more spread than for the other properties examined for these fluids. While the closest agreement for the configurational energy of real systems was for square-well fluids with $\lambda \approx 2$, the agreement for the isochoric heat capacity is closer for $\lambda \approx 1.5$. Again, the square-well system struggles to reproduce realistic behavior and has conflicting optimal well-widths depending on the chosen observable.

B. Mie *n*-6 fluids

Simulation data for the Zeno lines of the Mie n-6 fluids, taken from Ref. 44, are plotted Fig. 7. In general, these fluids are seen to follow the ideal Zeno line more closely than the square-well fluids. For all the Mie n-6 fluids explored, with the exception of $n = 8$, the Zeno lines curve downwards at higher density and lie below the ideal

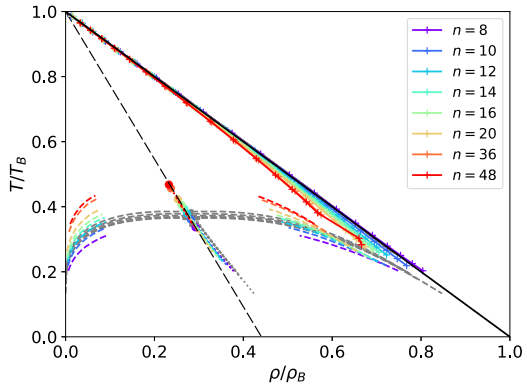

FIG. 7. The Zeno line for Mie *n*-6 fluids (colored solid lines) and real/corresponding-states fluids (gray solid lines). The dashed lines denote the boundaries of the vapor–liquid coexistence regions, and the dotted lines are the rectilinear diameters. The filled circles are the critical points for the Mie *n*-6 fluids, while the gray plus is the critical point for the corresponding state fluids. The data for the Zeno line and the coexistence curves for the Mie *n*-6 fluids were taken from the MD simulations of Refs. 10 and 44.

Zeno line. The Mie 8-6 fluid has the straightest Zeno line, but curves slightly upwards at large densities and lies above the 45° line.

Figure 8 shows a more detailed view of the Zeno line of the Mie *n*-6 fluids. This plot also includes the Zeno line for the Mie 11-6 fluid. As discussed previously, the curvature K of the Zeno line near zero density vanishes for $10 < n < 11$ (see Table I); however, only the Zeno line for $n = 8$ lies above the 45° line. This implies that, although the curvature is positive at zero density for $n = 10$, the curvature eventually becomes negative at higher densities, and the Zeno line dips below the 45° line. Hence, it is not expected that any of the Zeno lines for the Mie *n*-6 fluids will be straight.

In summary of the simulation results for the Zeno line, it is clear that both the Mie and square-well potentials can be optimized using their existing parameterizations to improve their agreement with real corresponding-states fluids; however, the current forms cannot maintain a straight Zeno line and thus deviate at higher densities. Optimal values of $\lambda = 1.8$ for square-wells and $n = 8$ to 10 for Mie *n*-6 fluids are suggested here, and Sec. V will explore if these values also provide good agreement with real fluids for the phase envelope.

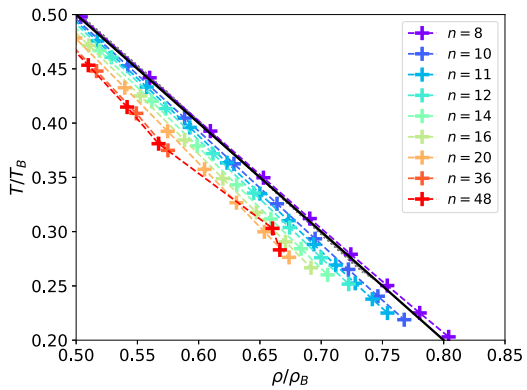

FIG. 8. The Zeno line for Mie *n*-6 fluids as in Fig. 7. The black line is the ideal Zeno line. The gray dashed lines are the Zeno lines for the corresponding states fluids.

V. VAPOR–LIQUID COEXISTENCE CURVES

As a basis for comparison of the vapor–liquid phase behavior of square-well and Mie fluids to real fluids, the following form proposed by Apfelbaum and Vorob'ev[16,23,25] was used, which was found to work well for a variety of experimental fluids:[16]

$$\frac{\rho_l}{\rho_B} = \frac{\rho_c}{\rho_B} + A\tau + B\tau^{\beta}, \tag{15}$$

$$A = \frac{T_c/T_B - \beta + \beta\rho_c/\rho_B}{1-\beta}, \tag{16}$$

$$B = \frac{(1 - T_c/T_B) - \rho_c/\rho_B}{1-\beta}, \tag{17}$$

where $\tau = 1 - T/T_c$. This form for the coexistence curve is based on the ansatz that the Zeno line is straight; that it should be tangent to the liquid branch of the vapor–liquid coexistence curve at low temperatures; and the universality of the shape of the coexistence curve near the critical point. In Fig. 9, the liquid branch of the vapor–liquid coexistence curve for various fluids is plotted. It can be observed that the form proposed by Apfelbaum and Vorob'ev [see Eq. (15)] provides a good description for the corresponding states fluids, which is expected.

A. Square-well fluids

The vapor–liquid coexistence envelopes for attractive square-well fluids with $\lambda = 1.5$ to 2, as determined from the multicanonical Monte Carlo simulations described in Sec. III, are plotted as the dashed lines in Fig. 3. When scaled by T_B and ρ_B, the coexistence curve broadens and shifts down to lower temperatures and higher

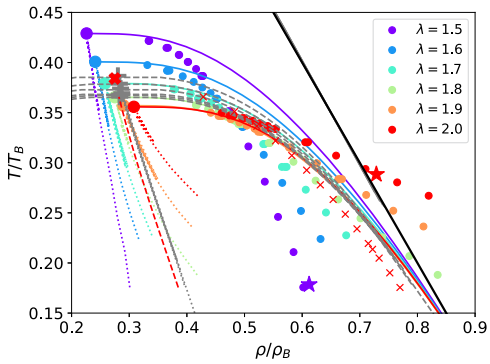

FIG. 9. The liquid branch of the vapor–liquid coexistence curve. The filled circles are the simulation data for square-well fluids. The red star denotes the triple point[53] for the square-well system with $\lambda = 2$; the purple star denotes the triple point[54] for $\lambda = 1.5$. The red crosses are simulation data for the Lennard-Jones 12-6 fluid.[9] The gray dashed lines are the coexistence curves for the corresponding states fluids. The solid lines are the predictions of the conjecture of Apfelbaum and Vorob'ev.[16,23,25]

densities as the well width λ increases. Again, the data for real fluids are plotted for comparison, as described in Fig. 1. In general, the square-well systems do not follow the form of Eq. (15), mainly due to the fact that the Zeno lines for these systems are not straight. For square-well fluids with a Zeno line that curves upward, the coexistence curve is broader than the proposed form, while for square-well fluids with a Zeno line that curves downward, the coexistence curve is narrower than the proposed form. It appears that the straighter the Zeno line of a system, the better its liquid branch, as described by Eq. (15). Despite this, the coexistence curve of these fluids is most similar to that of the square-well fluid with $\lambda = 1.8$, which is also the well width that has approximately the straightest Zeno line over the full density range (see Figs. 3 and 4).

Based on thermodynamic arguments,[55,56] the Zeno line should become tangent to the extension of the liquid branch of the vapor–liquid coexistence curve in the limit of zero temperature. Apfelbaum and Vorob'ev[16] observed that this appears to be the case for many experimental fluids.

For the range of conditions that we explore for the square-well fluids, we observe that the liquid branch of the coexistence curve never crosses the Zeno line. In general, for all λ, the curvature of Zeno lines increases with increasing density, and it appears that the Zeno line for each λ does indeed adjust to avoid intersecting the liquid branch of the vapor–liquid coexistence line; however, although it does appear that the Zeno lines could become tangent to the liquid branch of the vapor–liquid coexistence curve at low temperature, it will cross the freezing line before this can occur (see Ref. 24). Additionally, as λ increases, the Zeno line will intersect the freezing curve at higher scaled temperatures. For reference, the triple points for $\lambda = 2$ are $\rho_t\sigma^3 \approx 0.61$, $k_BT_t/\varepsilon \approx 2.16$, and $p_t\sigma^3/\varepsilon \approx 0.056$,[53] which correspond to the scaled values $\rho_t/\rho_B = 0.729$ and $T_t/T_B = 0.288$. This is given by the red star in Fig. 3. The triple points for $\lambda \approx 1.5$ were estimated[54] to be $\rho_l\sigma^3 \approx 0.835$, $k_BT_t/\varepsilon \approx 0.508$, and $p_t\sigma^3/\varepsilon \approx 0.000\,03$, which correspond to $\rho_t/\rho_B = 0.612$ and $T_t/T_B = 0.179$. This is denoted by the purple star.

To estimate the location of the critical temperature T_c and critical density ρ_c for square-well fluids, vapor–liquid coexistence data near the critical point are fit to the law of rectilinear diameter and the scaled form of the coexistence curve width,

$$\frac{\rho_l + \rho_g}{2\rho_c} = 1 + A\left(1 - \frac{T}{T_c}\right), \tag{18}$$

$$\rho_l - \rho_g = \rho_c B\left(1 - \frac{T}{T_c}\right)^{\beta}, \tag{19}$$

where ρ_g is the vapor density, ρ_l is the liquid density, A and B are fit parameters, and $\beta \approx 0.326\,53$ is the critical exponent of the three-dimensional Ising universality class.[57]

The results of the fits are reported in Table II. When scaled by the Zeno temperature T_B and density ρ_B, the critical temperature decreases, while the critical density increases with increasing well width. This can be observed in Fig. 3, where the critical points of the square-well fluid systems are denoted by filled circles. Apfelbaum and Vorob'ev observed that locus of critical points of monatomic fluids lies on a straight line, when scaled by the Zeno line parameters T_B and ρ_B (see Fig. 5 in Ref. 16). The scaled critical points of the square-well fluids are presented in Fig. 11 as filled black circles, along with the critical points of some experimental fluids. It was observed that the critical point of square-well fluids is most similar to that of the corresponding state fluids when the well width is in the range $1.8 \le \lambda \le 1.9$. Square-well fluids of this approximate well-width also give the best approximation of the straight Zeno line, as remarked earlier.

Here, it is observed that, unlike many real fluids, the square-well fluids do not follow the law of rectilinear diameter, as the mean of coexisting vapor and liquid densities do not vary linearly with temperature. The rectilinear diameters of the corresponding states and square-well fluids can be compared in Fig. 3. It can be observed that the rectilinear diameters of square-well fluids, in general, curve toward larger densities and only appear to be straight relatively near to the critical point. They do become more linear, however, as the well-width becomes smaller. We note that extremely close to the critical point, the rectilinear diameter is expected to possess a "hook" that is described by the universal scaling behavior[58–62] of fluids in the critical region. In this work, however, we are never sufficiently near to the critical point for this effect to be significant.

B. Mie *n*-6 fluids

Simulation data for the vapor–liquid coexistence curves for a range of Mie n-6 fluids with $n = 8$ to 48, taken from Ref. 44, are shown as the colored dashed lines in Fig. 7; the filled circles are the corresponding critical points. As n increases, the critical point moves up and to the left in nearly a straight line. The black dashed line connects the Boyle temperature to the critical point of the Mie 8-6 fluid. Interestingly, this line passes closely to critical points of all

TABLE II. Estimated critical constants and parameters of the rectilinear diameter for square-well fluids of varying width. Values are obtained from a range of system sizes, with smaller systems used for lower temperatures due to sampling issues with large density differences between phases.

λ	k_BT_c/ε	$\rho_c\sigma^3$	A	B	T_c/T_B	ρ_c/ρ_B
1.50	1.221 ± 0.001	0.308 ± 0.002	0.51 ± 0.09	3.61 ± 0.02	0.4290 ± 0.0002	0.226 ± 0.001
1.60	1.432 ± 0.000	0.283 ± 0.002	0.63 ± 0.10	3.56 ± 0.02	0.4007 ± 0.0001	0.241 ± 0.001
1.70	1.666 ± 0.001	0.269 ± 0.001	0.64 ± 0.08	3.54 ± 0.02	0.3792 ± 0.0002	0.258 ± 0.001
1.80	1.943 ± 0.001	0.261 ± 0.002	0.64 ± 0.15	3.51 ± 0.03	0.3654 ± 0.0002	0.275 ± 0.002
1.90	2.266 ± 0.001	0.255 ± 0.002	0.85 ± 0.14	3.57 ± 0.03	0.3571 ± 0.0002	0.290 ± 0.002
2.00	2.664 ± 0.001	0.258 ± 0.002	1.05 ± 0.18	3.60 ± 0.03	0.3558 ± 0.0002	0.308 ± 0.002

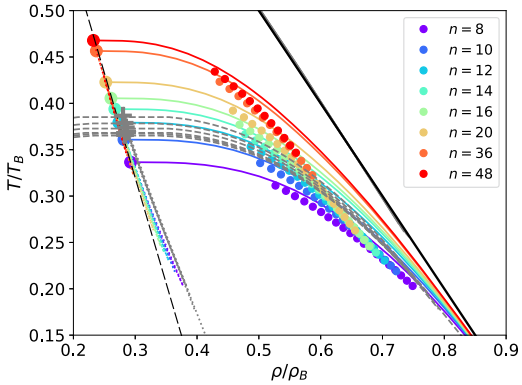

FIG. 10. The liquid branch of the vapor–liquid coexistence curve for Mie n-6 fluids. The filled circles are simulation data from Ref. 44. The solid lines are the predictions of the conjecture of Apfelbaum and Vorob'ev.[16,23,25]

the examined Mie n-6 fluids, although it lies slightly to the right of these fluids. The dotted lines are the rectilinear diameters of the various fluids; these are fairly straight for the Mie n-6 fluids. For $n = 48$, the rectilinear diameter has a slope such that it passes through the critical points of the other Mie n-6 fluids. As n decreases, the slope becomes less steep and becomes similar to that of the corresponding state fluids.

As with the square-well fluids, the liquid branches of the coexistence curves for the Mie n-6 fluids do not cross their respective Zeno lines. As the Zeno lines curve further downward for larger values of n, the coexistence curves of the Mie n-6 fluids become more narrow as n increases. In Fig. 10, the liquid branches of the vapor–liquid coexistence curves for several Mie n-6 fluids are plotted. The liquid branch of the Mie fluids is consistently more narrow than the form given in Eq. (15).

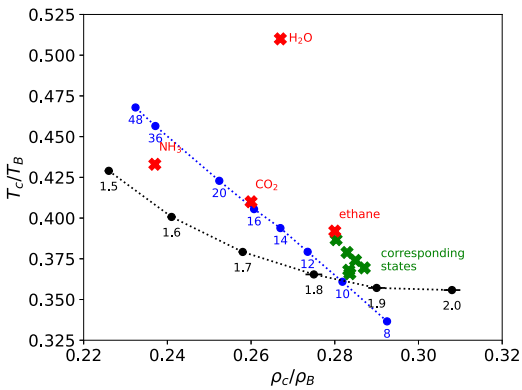

FIG. 11. The critical point for various fluids. The black filled circles are for square-well of different well widths λ; the dotted lines are a guide for the eyes. The blue numbers are for Mie n-6 systems, where the number is the value of n; the simulation data for the critical points for these systems were taken from Ref. 44, and the Zeno line parameters were taken from Ref. 24. The critical points for Mie n-6 fluids are given by the blue numbers, which denote the value of n [see Eq. (1)]; the data were taken from Table II of Ref. 24, which computed the Zeno line parameters T_B and ρ_B and compiled the simulation data for the critical point from a variety of sources.[63–67] The green crosses are for the corresponding states fluids, and the red crosses are for different real fluids; data taken from Ref. 8.

The scaled critical points of the Mie n-6 fluids are presented in Fig. 11 as blue filled circles. As the repulsive core of the potential becomes softer (i.e., smaller the value of n), the scaled critical temperature decreases, and the scaled critical density increases, which is consistent with Fig. 7. As was observed for the square-well fluids, the Mie fluid that most closely replicates the critical point of the corresponding states fluids is that which provides the straightest Zeno line (i.e., $8 \le n \le 10$).

With the exception of water which is known to behave unusually in comparison to other fluids, it should be noted that these fluids lie in the same general region as the square-well and Mie fluids. It is possible then that the vapor–liquid phase behavior of different experimental fluids can be replicated using simple pair-potential fluids within reasonable bounds, provided that the free parameters of the fluid are selected carefully.

VI. CONCLUSIONS

In this work, the Zeno line and its relation to the vapor–liquid coexistence behavior are examined in detail for attractive square well fluids of varying widths and Mie n-6 fluids with repulsive cores of varying steepness.

The properties of the Zeno line at low density can be determined directly from the virial coefficients. In particular, the curvature of the Zeno line at zero density can be determined directly from knowledge of the second, third, and fourth virial coefficients [see Eq. (8)]. By examining the curvature, it is found that, in general, the Zeno line is not straight for molecular fluids that interact through model potentials. This implies that, in general, the Zeno line is not straight for systems with any generic interaction potential and only specific interaction potentials may possess a straight Zeno line.

For square-well fluids, event-driven molecular dynamics are performed to establish the Zeno line, and multicanonical Monte Carlo simulations are used to determine the phase behavior. For short well-widths with $\lambda < 1.896$, the Zeno line has an initially negative curvature at zero density, while for large well widths with $\lambda > 1.896$, the Zeno line has a positive initial curvature. As the density increases (or, equivalently, the temperature decreases), the curvature of the Zeno lines increases so that they all become positive at the highest densities. The coexistence curves of the square-well fluid move to lower scaled temperatures and broaden as the well width increases. In all cases, the liquid branch never crosses the Zeno line and, instead, appears to approach it as a tangent.

While none of the square-well fluids have a perfectly straight Zeno line, the well width $\lambda \approx 1.8$ presents a reasonably straight Zeno line and a phase coexistence curve that is most similar to that of experimental fluids that obey the law of corresponding states (see Fig. 3). Perhaps surprisingly, this square-well fluid matches the phase behavior of the corresponding state systems more closely than the Lennard-Jones 12-6 system.

The Zeno lines and coexistence behavior for the Mie n-6 fluids were taken from MD simulation data in Refs. 10 and 44. As with the square-well fluids, none of the Zeno lines for the Mie fluids investigated in this work are entirely straight (Fig. 8). Mie n-6 fluids with $n \ge 11$ have negative curvature at zero density, while those with $n \le 10$ have a positive curvature. Of the fluids studied, all the Zeno lines curve downward at high densities, with the exception of $n = 8$, which curves upward. The scaled coexistence

curves of the Mie n-6 fluids move to lower temperatures and become broader as n decreases (i.e., the repulsive core becomes "softer"). The coexistence curves are all more narrow than that of the corresponding state fluids. As with the square-well fluids, the liquid branch of the coexistence curve appears to approach a tangent to the Zeno line.

Therefore, general interaction potentials do not lead to the regularities observed in the thermodynamic properties of real fluids. This raises the question as to why real systems, which possess exceptionally complex, multibody intermolecular forces, exhibit these regularities in their thermodynamic properties, while simple pair potentials do not.

For example, many nearly spherical molecules (e.g., argon, xenon, krypton, methane, nitrogen, and oxygen) follow the law of corresponding states,[3,4] where their thermodynamic properties can be collapsed into a universal curve by rescaling by their critical properties. This collapse is sometimes attributed to the fact that they are non-polar and spherically symmetric; however, this cannot be the reason, as model fluids with short-ranged, spherically symmetric pair potentials cannot generally be scaled onto each other, as evidenced by the model systems explored here.

This observation can be rationalized within the renormalization group (RG) framework,[68,69] which involves a transformation where the degrees of freedom of a system are sequentially integrated over increasing large length scales, and then scaled back down. The RG transformation maintains the free energy (partition function) of the system, but will alter its effective interactions (e.g., the transformation will generate multi-body interactions in a system that originally had only pair-wise interactions). This process can be viewed as generating a trajectory that passes through systems with different interaction potentials, all of which will have the same equilibrium large-scale structure (e.g., scattering function at low angles) and thermodynamic behavior. The interaction potential of a particular real fluid would correspond to a single point on one of these trajectories. Note that there are many different trajectories depending on the starting system.

The regularities that are observed in the thermodynamic properties of real fluids fundamentally arise from the fact that the intermolecular forces have a common origin in the electrostatic interactions and correlated fluctuations between electrons and atomic nuclei. Fluids with phase coexistence behavior that collapse onto the same corresponding states class would be expected to lie on the same RG trajectory and therefore have the same, scaled thermodynamic properties. An interesting feature of many of the RG trajectories that correspond to real fluids is a straight Zeno line.

This raises the possibility that there may be certain forms of the two-body potential that lie on, or very near to, a RG trajectory of a real fluid. These potentials would reproduce the thermodynamic properties and large scale structure of the real fluid across a very broad range of conditions. Not all forms of the potential would satisfy this, but only very specific choices. It is possible, then, that one such criterion for finding effective pair-potentials, which lie on the RG trajectory of the corresponding state fluids, is a straight Zeno line. This motivates the search for spherically symmetric potentials that have straight Zeno lines. To somewhat limit the scope of the search, a further constraint is that the potentials must ensure that the curvature of the Zeno line is zero at low densities [see Eq. (8)] through their virial coefficients.

To provide a preliminary example of the use of these Zeno properties, calculations for the Zeno line at low densities were performed on three detailed force fields for argon. The first force field is a pair-wise additive model developed by Jager and co-workers.[70,71] The second model also uses this two-body potential but includes an additional three-body potential developed by Axilrod, Teller, and Muto;[72,73] we refer to this as the ATM model. The final force field takes the same two-body potential but adds an improved three-body potential model developed by Jager *et al.*[70,71] The virial coefficients for each of these models were calculated by Jager *et al.*[74] The Boyle temperature of all three models is $T_B = 408.566$ K, which corresponds to $T_c/T_B = 0.3688$. This should be compared to the experimental value[8] of $T_B = 407.93$ K, which corresponds to $T_c/T_B = 0.369$.

The Zeno density for the pair-wise additive model is $\rho_B = 52.67$ mol l^{-1}, which corresponds to $\rho_c/\rho_B = 0.2545$ and $K = -0.027\,67$. For the ATM model, $\rho_B = 45.48$ mol l^{-1} ($\rho_c/\rho_B = 0.2948$) and $K = 0.1041$. For the non-additive model of Jager and co-workers,[70,71] $\rho_B = 45.04$ mol l^{-1} ($\rho_c/\rho_B = 0.2977$) and $K = 0.1089$. The experimental value[8] for the Zeno density is $\rho_B = 46.71$ mol l^{-1} ($\rho_c/\rho_B = 0.287$). The quantity ρ_B requires knowledge of the third virial coefficient, which depends on the three-body potential. It is interesting to note that including the three-body potential significantly improves the estimation of the Zeno density.

The zero density curvature K of the Zeno line depends on the fourth virial coefficient, which depends on the four-body potential. All of the three force fields examined had a curvature greater in magnitude than that of the Lennard-Jones 12-6 potential, although we expect that the experimental value of K should be very close to zero. None of the models had a four-body interaction, and one might expect that if an accurate approximation were included in the force field, this would lead to a value of K close to zero.

To describe experimental fluids in other corresponding state classes, such as those with non-zero acentric factors, such as carbon dioxide or linear alkanes, it is anticipated that a non-spherical pair-wise additive potential will be required. We expect there to be many non-spherically symmetric pair potentials that lead to fluids that possess a straight Zeno line. It would be interesting to explore fluids composed of linear chains of particles that interact through spherically symmetric potentials to see if any have straight Zeno lines and how these fluids relate to the corresponding real fluids. This would help to explore some of the origin of the straight Zeno line and has implications for the development of coarse grained potentials.

SUPPLEMENTARY MATERIAL

The supplementary material includes figures containing Zeno lines for square-well and Mie n-6 fluids scaled by their critical temperatures and densities, a comparison of the calculated vapor–liquid phase envelopes for square-well fluids to that of other works, and tabulated vapor–liquid coexistence data for square-well fluids.

ACKNOWLEDGMENTS

The authors gratefully acknowledge the financial support from CCP5.

AUTHOR DECLARATIONS

Conflict of Interest

The authors have no conflicts to disclose.

Author Contributions

Thomas Paterson: Data curation (equal); Formal analysis (equal); Investigation (equal); Software (equal); Writing – original draft (equal); Writing – review & editing (equal). **Marcus N. Bannerman**: Conceptualization (equal); Data curation (equal); Formal analysis (equal); Investigation (equal); Software (equal); Writing – original draft (equal); Writing – review & editing (equal). **Leo Lue**: Conceptualization (equal); Data curation (equal); Formal analysis (equal); Investigation (equal); Software (equal); Supervision (equal); Writing – original draft (equal); Writing – review & editing (equal).

DATA AVAILABILITY

The data that support the findings of this study are available from the corresponding author upon reasonable request.

APPENDIX: EXPRESSION FOR THE VIRIAL COEFFICIENTS FOR SQUARE-WELL FLUIDS

In this appendix, explicit expressions are given for the second, third, and fourth virial coefficients that are used in this work. The second virial coefficient B_2 is known exactly for square well systems[34–36] and is given by the following expression:

$$B_2(T)/B_2^{\mathrm{HS}} = 1 - (\lambda^3 - 1)\Delta, \tag{A1}$$

where $\Delta = e^{\beta\epsilon} - 1$, $\beta = (k_B T)^{-1}$, k_B is the Boltzmann constant, and $B_2^{\mathrm{HS}} = 2\pi\sigma^3/3$ is the second virial coefficient of a hard sphere with diameter σ.

The third virial coefficient B_3 is also known exactly[34–36] and is given by

$$B_3(T)/[B_2^{\mathrm{HS}}]^2 = \frac{5}{8}[1 - \Delta f_1(\lambda) - \Delta^2 f_2(\lambda) - \Delta^3 f_2(\lambda)], \tag{A2}$$

where the functions $f_n(\lambda)$ are given by

$$f_1(\lambda) = \begin{cases} 0 & \text{for } \lambda \le 1, \\ \frac{1}{5}(\lambda^6 - 18\lambda^4 + 32\lambda^3 - 15) & \text{for } 1 < \lambda \le 2, \\ \frac{17}{5} & \text{for } 2 < \lambda, \end{cases} \tag{A3}$$

$$f_2(\lambda) = \begin{cases} 0 & \text{for } \lambda \le 1, \\ \frac{2}{5}(\lambda^6 - 18\lambda^4 + 16\lambda^3 + 9\lambda^2 - 8) & \text{for } 1 < \lambda \le 2, \\ \frac{1}{5}(-32\lambda^3 + 18\lambda^2 + 48) & \text{for } 2 < \lambda, \end{cases} \tag{A4}$$

$$f_3(\lambda) = \begin{cases} 0 & \text{for } \lambda \le 1, \\ \frac{6}{5}(\lambda^2 - 1)^3 & \text{for } 1 < \lambda \le 2, \\ \frac{1}{5}(5\lambda^6 - 32\lambda^3 + 18\lambda^2 + 26) & \text{for } 2 < \lambda. \end{cases} \tag{A5}$$

TABLE III. Parameters for the fourth virial coefficient of square-well potential.[31]

j	p_{4j0}	$p_{4j'}$	p_{4j2}	p_{4j3}
0	1.147 798	0	0	0
1	−1.686 92	2.004	3.166 19	−2.394 46
2	1.732 86	−0.848 474	−7.272 83	3.283 37
3	−2.3932	−3.172 96	10.1419	−0.915 451
4	3.987 45	3.110 22	7.247 59	−9.608 72
5	−3.161 46	−8.721 17	−4.294 17	−6.296 75
6	−2.3078	−1.089 52	−5.700 65	0.608 232

There is no analytical expression for the fourth virial coefficient; however, approximate expressions for the fourth, fifth, and sixth virial coefficients have been provided by Elliott and co-workers[31] for $1.2 \le \lambda \le 2.0$. The nth order virial coefficient $B_n(T)$ is given in the following form:

$$B_n(T) = v_0^{n-1} \sum_{j=0}^{n(n-1)/2} \hat{B}_{nj}(\lambda)\Delta^j, \tag{A6}$$

where $v_0 = \pi\sigma^3/6$ is the volume of a sphere of diameter σ and the functions $\hat{B}_{nj}(\lambda)$ are

$$\hat{B}_{nj}(\lambda) = \binom{j_{\max}}{j}(\lambda - 1)^j n^2 \max(j, 1)\hat{B}_{nj}^{\mathrm{red}}(\lambda), \tag{A7}$$

with $\hat{B}_{nj}^{\mathrm{red}}(\lambda)$ given by

$$\hat{B}_{nj}^{\mathrm{red}}(\lambda) \approx p_{nj0} + p_{nj1}(\lambda - 1) + p_{nj2}(\lambda - 1)^2 + p_{nj3}(\lambda - 1)^3. \tag{A8}$$

The values of the parameters p_{njk} for the fourth virial coefficient are shown in Table III.

REFERENCES

[1] L. Cailletet and E. C. Mathias, C. R. Acad. Sci. **102**, 1202 (1886).
[2] J. V. Sengers and J. M. H. L. Sengers, Annu. Rev. Phys. Chem. **37**, 189–222 (1986).
[3] K. S. Pitzer, J. Am. Chem. Soc. **77**, 3427 (1955).
[4] K. S. Pitzer, D. Z. Lippmann, R. F. Curl, C. M. Huggins, and D. E. Petersen, J. Am. Chem. Soc. **77**, 3433 (1955).
[5] E. M. Holleran, J. Chem. Phys. **47**, 5318 (1967).
[6] J. Xu and D. R. Herschbach, J. Phys. Chem. **96**, 2307 (1992).
[7] H. E. Stanley, *Introduction to Phase Transitions and Critical Phenomena*, *International Series of Monographs on Physics* (Clarendon Press, Oxford, 1971).
[8] P. Linstrom, NIST Chemistry WebBook: NIST Standard Reference Database 69, 1997.
[9] D. Siderius, NIST Standard Reference Simulation Website SRD 173, 2017.
[10] M. Urschel and S. Stephan, J. Chem. Theory Comput. **19**, 1537–1552 (2023).
[11] J. J. Potoff and A. Z. Panagiotopoulos, J. Chem. Phys. **109**, 10914–10920 (1998).
[12] A. Ahmed and R. J. Sadus, J. Chem. Phys. **131**, 174504 (2009).
[13] A. Ahmed and R. J. Sadus, J. Chem. Phys. **133**, 229902 (2010).
[14] D. Ben-Amotz and D. R. Herschbach, Isr. J. Chem. **30**, 59 (1990).
[15] V. L. Kulinskii, J. Phys. Chem. B **114**, 2852 (2010).
[16] E. M. Apfelbaum and V. S. Vorob'ev, J. Phys. Chem. B **112**, 13064 (2008).
[17] I. H. Umirzakov, J. Phys. Chem. B **121**, 4945 (2017).
[18] I. C. Sanchez, S. O'Keefe, and J. F. Xu, J. Phys. Chem. B **120**, 3705 (2016).

[19] A. Batschinski, Ann. Phys. **324**, 310 (1906).
[20] M. C. Kutney, M. T. Reagan, K. A. Smith, J. W. Tester, and D. R. Herschbach, J. Phys. Chem. B **104**, 9513 (2000).
[21] A. Maghari and L. Hosseinzadeh-Shahri, Fluid Phase Equilib. **206**, 287 (2003).
[22] A. Maghari and Z. Safaei, J. Mol. Liq. **142**, 95 (2008).
[23] E. M. Apfelbaum and V. S. Vorob'ev, J. Phys. Chem. B **113**, 3521 (2009).
[24] E. M. Apfelbaum and V. S. Vorob'ev, J. Chem. Phys. **130**, 214111 (2009).
[25] E. M. Apfelbaum and V. S. Vorob'ev, Chem. Phys. Lett. **467**, 318 (2009).
[26] E. Apfelbaum, J. Mol. Liq. **334**, 116088 (2021).
[27] E. M. Apfelbaum, J. Phys. Chem. B **126**, 2912 (2022).
[28] U. K. Deiters and A. Neumaier, J. Chem. Eng. Data **61**, 2720–2728 (2016).
[29] S. Stephan and U. K. Deiters, Int. J. Thermophys. **41**, 147 (2020).
[30] J. O. Hirschfelder, C. F. Curtiss, and R. B. Bird, *Molecular Theory of Gases and Liquids* (Wiley, 1954).
[31] J. R. Elliott, A. J. Schultz, and D. A. Kofke, J. Chem. Phys. **143**, 114110 (2015).
[32] J. M. Smith, H. C. V. Ness, M. M. Abbott, and M. T. Swihart, *Introduction to Chemical Engineering Thermodynamics* (McGraw-Hill, New York, NY, 2022).
[33] E. M. Holleran, J. Chem. Phys. **49**, 39–43 (1968).
[34] T. Kihara, Rev. Mod. Phys. **25**, 831 (1953).
[35] J. A. Barker and J. J. Monaghan, J. Chem. Phys. **36**, 2558–2563 (1962).
[36] S. B. Kiselev, J. F. Ely, L. Lue, and J. R. Elliott, Fluid Phase Equilib. **200**, 121 (2002).
[37] S. Katsura, Phys. Rev. **115**, 1417 (1959).
[38] S. Katsura, J. Chem. Phys. **45**, 3480–3482 (1966).
[39] J. A. Barker and D. Henderson, Can. J. Phys. **45**, 3959–3978 (1967).
[40] H. Do, C. Feng, A. J. Schultz, D. A. Kofke, and R. J. Wheatley, Phys. Rev. E **94**, 013301 (2016).
[41] M. Gottschalk, AIP Adv. **9**, 125206 (2019).
[42] A. J. Schultz, "Etomica website: B_2 via quadrature and series expansion," https://www.etomica.org/apps/virial/b2 (2005) (accessed November 18, 2023).
[43] A. J. Schultz, "Etomica website: Virial coefficients via mayer-sampling Monte Carlo," https://www.etomica.org/apps/virial/msmc, 2005 (accessed November 18, 2023).
[44] S. Stephan and M. Urschel, J. Mol. Liq. **383**, 122088 (2023).
[45] M. N. Bannerman, R. Sargant, and L. Lue, J. Comput. Chem. **32**, 3329 (2011).
[46] M. N. Bannerman and L. Lue, J. Chem. Phys. **133**, 124506 (2010).
[47] J. Buchner, Stat. Comput. **26**, 383 (2016).
[48] J. Buchner, Publ. Astron. Soc. Pac. **131**, 108005 (2019).
[49] J. Buchner, Stat. Surv. **17**, 169–215 (2023).
[50] N. B. Wilding, Phys. Rev. E **52**, 602 (1995).
[51] G. Orkoulas and A. Z. Panagiotopoulos, J. Chem. Phys. **110**, 1581–1590 (1999).
[52] N. B. Wilding, Am. J. Phys. **69**, 1147 (2001).
[53] C. G. Pruteanu, M. N. Bannerman, M. Kirsz, L. Lue, and G. J. Ackland, ACS Omega **8**, 12144 (2023).
[54] H. Liu, S. Garde, and S. Kumar, J. Chem. Phys. **123**, 174505 (2005).
[55] E. M. Apfelbaum, V. S. Vorob'ev, and G. A. Martynov, J. Phys. Chem. B **110**, 8474 (2006).
[56] L. P. Filippov, *Metody rascheta i prognozirovaniya svoistv veshchestv (Methods for Calculating and Predicting the Properties of Substances)* (Izd-vo MGU, Moscow, 1988).
[57] M. Campostrini, A. Pelissetto, P. Rossi, and E. Vicari, Phys. Rev. E **65**, 066127 (2002).
[58] B. Widom and J. S. Rowlinson, J. Chem. Phys. **52**, 1670–1684 (1970).
[59] S. Jüngst, B. Knuth, and F. Hensel, Phys. Rev. Lett. **55**, 2160 (1985).
[60] R. R. Singh and K. S. Pitzer, J. Chem. Phys. **92**, 3096–3099 (1990).
[61] Y. C. Kim, Phys. Rev. E **71**, 051501 (2005).
[62] Y. Garrabos, C. Lecoutre, S. Marre, D. Beysens, and I. Hahn, Phys. Rev. E **97**, 020101 (2018).
[63] H. Okumura and F. Yonezawa, J. Chem. Phys. **113**, 9162–9168 (2000).
[64] A. Z. Panagiotopoulos, J. Chem. Phys. **112**, 7132–7137 (2000).
[65] I. Charpentier and N. Jakse, J. Chem. Phys. **123**, 204910 (2005).
[66] G. Galliéro, C. Boned, A. Baylaucq, and F. Montel, Phys. Rev. E **73**, 061201 (2006).
[67] P. Orea, Y. Reyes-Mercado, and Y. Duda, Phys. Lett. A **372**, 7024–7027 (2008).
[68] N. Goldenfeld, *Lectures on Phase Transitions and the Renormalization Group* (Addison-Wesley, Reading, MA, 1992).
[69] J. Cardy, *Scaling and Renormalization in Statistical Physics* (Cambridge University Press, Cambridge, 1996).
[70] B. Jäger, R. Hellmann, E. Bich, and E. Vogel, Mol. Phys. **107**, 2181–2188 (2009).
[71] B. Jäger, R. Hellmann, E. Bich, and E. Vogel, Mol. Phys. **108**, 105 (2010).
[72] B. M. Axilrod and E. Teller, J. Chem. Phys. **11**, 299–300 (1943).
[73] Y. Muto, J. Phys. Math. Soc. Jpn. **17**, 629 (1943).
[74] B. Jäger, R. Hellmann, E. Bich, and E. Vogel, J. Chem. Phys. **135**, 084308 (2011).